Cooperation of Hot Holes and Surface Adsorbates in Plasmon-Driven Anisotropic Growth of Gold Nanostars

Wenxiao Guo,[†] Aaron C. Johnston-Peck,[‡] Yuchao Zhang,[†, §] Yue Hu,[†] Jiawei Huang,[†] and Wei David Wei[†]*

[†]Department of Chemistry and Center for Catalysis, University of Florida, Gainesville, Florida 32611, United States

[‡]Material Measurement Laboratory, National Institute of Standards and Technology, 100 Bureau Drive, Gaithersburg, Maryland 20899, United States

*Address correspondence to wei@chem.ufl.edu

ABSTRACT: Light-driven synthesis of plasmonic metal nanostructures has garnered broad scientific interests. Although it has been widely accepted that surface plasmon resonance (SPR)-generated energetic electrons play an essential role in this photochemical process, the exact function of plasmon-generated hot holes in regulating the morphology of nanostructures has not been fully explored. Herein, we discover that those hot holes work with surface adsorbates collectively to control the anisotropic growth of gold (Au) nanostructures. Specifically, it is found that hot holes stabilized by surface adsorbed iodide enable the site-selective oxidative etching of Au^0, which leads to nonuniform growths along different lateral directions to form six-pointed Au nanostars. Our studies establish a molecular-level understanding of the mechanism behind the plasmon-driven synthesis of Au nanostars and illustrate the importance of cooperation between charge carriers and surface adsorbates in regulating the morphology evolution of plasmonic nanostructures.

Plasmon-driven growth of noble metal nanostructures has garnered extensive scientific interests in the past two decades.[1-9] Previous studies have shown that the excitation of surface plasmon resonance (SPR) on seed nanoparticles produces energetic (or "hot") electrons to drive the photochemical reduction of precursors and form various anisotropic noble metal nanostructures.[6-7, 9-15] Nevertheless, it is noted that in reported processes of Au nanostructure synthesis, the potential of hot holes (the counterparts of hot electrons) for tuning the morphology evolution still remains elusive.

Herein, we found that those plasmon-generated hot holes worked cooperatively with surface adsorbates to control the anisotropic growth of Au nanostructures. Under visible-light irradiation, the addition of iodide into a growth solution containing planar-twinned Au seeds produced six-pointed Au nanostars instead of regular nanoprisms.[7] Further studies showed that those Au nanostars were formed only under irradiation in the shorter-wavelength region (i.e., < 600 nm) of Au SPR that generated highly energetic interband holes, suggesting a hot-hole-driven process in photochemical reactions. Additionally, photoelectrochemical studies showed enhancements in both the anodic open-circuit potential (OCP) shift and the oxidative photocurrent on a Au nanocrystal electrode in the presence of iodide. These observations demonstrated that the coupling between surface-adsorbed iodide and hot holes facilitated the hot-hole-driven surface etching of Au. Moreover, the examination of morphology evolution of intermediate Au nanostructures during the growth confirmed that preferential hot-hole-driven etching occurred on edges exposing more high-index facets, which caused nonuniform lateral growths and eventually led to the formation of Au nanostars. Taken together, our results established a clear picture of the essential role of hole-adsorbate cooperation in governing photochemical processes and enabling the control of nanostructure morphology in plasmon-driven synthesis.

In a typical experiment, a growth solution was irradiated at 520 ± 10 nm (i.e., the SPR band of Au seeds)[7, 9, 13] for 20 min. Then, potassium iodide (KI, 4 μM) was added and the mixture was irradiated continuously for another 60 min. Interestingly, six-pointed Au nanostars with tip-to-tip length around 437 ± 30 nm (Figures 1A and S2A) were formed instead of previously reported regular Au nanoprisms.[6-7] Au nanostars showed a broad absorption in the

near-infrared region (Figure S2B).The selected area electron diffraction (SAED) pattern of a flat-lying Au nanostar (Figure S2C) was indexed to a [111] zone axis, suggesting that Au nanostars were single crystals bound by {111} facets on top and bottom faces. Further studies showed that similar Au nanostars were produced when replacing KI with sodium iodide (NaI, Figure S3A). Meanwhile, only regular Au nanoprisms were found in the absence of iodide (Figure S3B). Both results strongly suggested that iodide was necessary for forming Au nanostars.

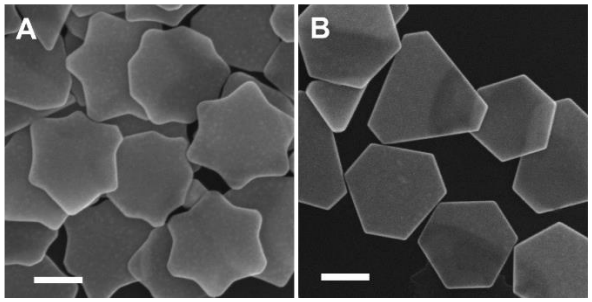

Figure 1. Scanning electron microscopy (SEM) images of Au nanostructures obtained from plasmon-driven growth of planar twinned Au seeds in the presence of iodide. (A) Six-pointed Au nanostars formed under 520 ± 10 nm irradiation (3.4 mW/cm^2). (B) Regular Au nanoprisms formed under 640 ± 10 nm irradiation (3.4 mW/cm^2). Scale bars in both (A) and (B) stand for 200 nm.

Iodide is commonly used to passivate the growth of Au {111} facets for controlling the morphology of Au nanostructures in wet synthesis.[16-21] However, the aforementioned growth solution only generated regular Au nanoprisms in the dark (Figure S3C), suggesting that the facet passivation by iodide should not govern the morphology evolution of Au nanostars. Thus, the formation of Au nanostars should arise from the participation of both iodide and the SPR excitation. It is noted that the SPR excitation generates three effects on Au nanoparticles: hot electron-hole pairs, enhanced local electromagnetic (EM) fields, and photothermal heating.[22-24] Under steady-state conditions, the high thermal conductivity of Au should create a homogeneous temperature distribution along Au seed nanoparticles,[25,26] making photothermal heating impossible to drive the anisotropic growth. Meanwhile, the symmetry of Au nanostars was found to be different from that of distribution of enhanced local EM fields excited by non-polarized light sources used in our study.[7, 27] Therefore, the formation of Au nanostars must involve hot-carrier-driven processes associated with iodide.

Interestingly, the formation of Au nanostars only occurred when irradiating the growth solution with shorter wavelengths of Au SPR (< 600 nm, Figures S4A – S4E). Using longer wavelengths (> 600 nm) solely produced regular Au nanoprisms (Figures 1B, and S4F – S4H). It has been known that the SPR excitation of Au nanoparticles prompts both intraband (sp → sp) and interband (d → sp) transitions with interband transitions being dominant at shorter wavelengths.[28-34] Intraband transitions distribute a larger portion of photon energy to hot electrons and generate lukewarm holes, while interband transitions generate a larger population of highly energetic d-band holes coupled with relatively less energetic electrons.[28-34] Nevertheless, both types of plasmon-generated hot electrons carry energies above the Fermi level of Au nanoparticles (0.7 V vs. normal hydrogen electrode, NHE) that is well above the reduction potential of $AuCl_4^-$ (1.002 V vs. NHE), making hot-electron-driven processes unlikely to have such an energy (i.e., wavelength) cut-off. Taken together, the coincidence of the observed wavelength dependence of nanostar formation and the interband transition threshold (ca. 2 eV, 620 nm)[30, 32-33] implied that those hot holes generated via interband transitions should work together with iodide to determine the formation of Au nanostars.

Iodide has been known as a hole-mediator in dye-sensitized solar cells, and the hot-hole-driven oxidative etching has been reported for the dissolution of Au and Ag nanostructures.[35-42] Thus, it is very likely that iodide in the growth solution strongly adsorbed on the surface of Au seed nanoparticles to form Au-iodide species;[43-44] plasmon-generated hot holes were then trapped and stabilized on the adsorbed iodide and drove the oxidative etching of Au^0. It is noted that iodide would also form stable complexes with Au^+ and Au^{3+} ions to accelerate the oxidative etching of Au^0.[45]

The collective interaction between hot holes and iodide was verified by an anodic shift of OCP on a Au nanocrystal electrode pre-adsorbed with iodide under irradiation (Figure 2A). It is noted that the photo-driven OCP shift reflects the sign of electrolyte ions attached to the electrode.[46-47] Thus, plasmon-generated hot holes were trapped and localized by surface Au-iodide species, while hot electrons were accumulated on the Au electrode and attracted cations from the bulk electrolyte, leading to the anodic OCP shift. This is in contrast to the cathodic OCP shift observed on an Au electrode adsorbed with electron-trapping polyvinylpyrrolidone (PVP) (Figure 2A).[6-7]

Furthermore, an oxidation peak at ca. 0.95 V vs. reversible hydrogen electrode (RHE) appeared in the linear sweep voltammetry (LSV) scan of an iodide-adsorbed Au nanocrystal electrode (Figure S5), corresponding to the one-electron oxidation of Au^0 to AuI_2^-.[48] Moreover, chronoamperometry (I-t) measurements showed an enhanced steady-state anodic photocurrent in the presence of iodide (Figure 2B), confirming that the cooperative interaction between hot holes and iodide facilitated the oxidative etching of Au^0.

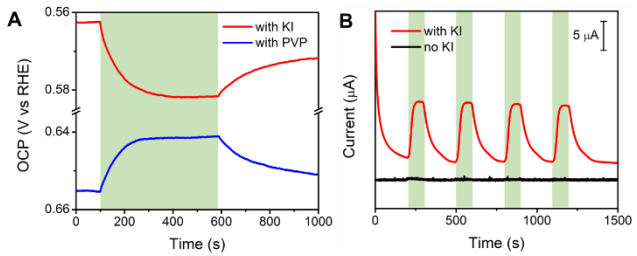

Figure 2. (A) OCP of Au nanocrystal electrode in the presence of 120 μM KI (red curve) and PVP (blue curve), respectively. The anodic change of an iodide-adsorbed Au electrode upon irradiation (shaded region) suggested that plasmon-generated hot holes were trapped and localized by surface Au-iodide species while hot electrons accumulated on the Au electrode and attracted cations from the bulk electrolyte. In contrast, the cathodic change on a PVP-adsorbed Au electrode suggested the attraction of anions from the bulk electrolyte by hot holes due to the trapping of hot electrons by PVP. (B) Chronoamperometry (I-t) of Au nanocrystal electrode at 1.03 V vs. RHE in the presence of 120 μM KI (red curve) and no KI (black curve). Shaded regions in both (A) and (B) represent the light irradiation using 530 ± 10 nm LED (240 mW/cm^2).

The examination of shape evolution of Au seed nanoparticles revealed that the hot-hole-driven oxidative etching of Au^0 assisted by iodide played an important role in the formation of Au nanostars. It should be noted that due to the strong affinity of iodide to Au,[43-44] iodide should adsorb across the whole surface of Au seed nanoparticles and facilitate the etching of Au^0 at all exposed sites on growing Au nanostructures. However, the etching rate varied on different sites with different coordination numbers, and atoms with lower coordination numbers were less stable, thus exhibiting faster oxidative etching.[49-51] As shown in Figure 3A and Figure S6A, small hexagonal nanoprisms with edges mainly consisted of low-index Au {100} and Au {111} facets were formed in the initial 20-min iodide-free growth.[4] Such a lateral growth was previously identified as a result of hot-electron-driven Au^0 deposition assisted by PVP adsorbed along edges of planar-twinned Au seeds.[7] When KI was added for a 30-min growth, the size of those nanoprisms kept increasing, but their corners became truncated, forming dodecagonal structures with six edges preserved from initial hexagonal nanoprisms and six new edges intersecting original ones (Figures 3B, 3D, S6B, and S6D). The overall increase in size came from the hot-electron-driven deposition of Au^0, while the truncation of Au nanoprism corners resulted from the faster hot-hole-driven etching of Au^0 due to their lower coordination numbers.

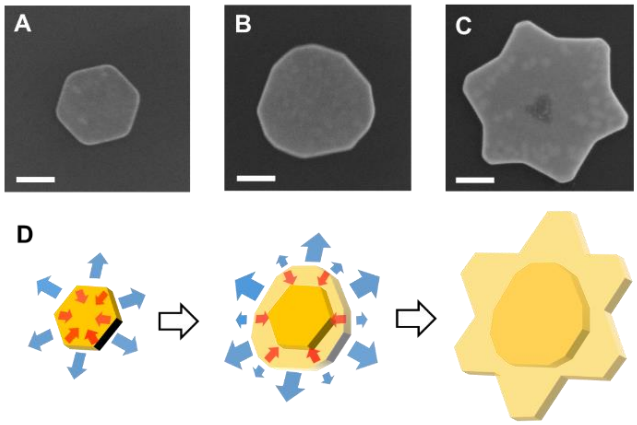

Figure 3. Morphology evolution of Au nanostructures during the plasmon-driven growth. (A) A SEM image of Au hexagonal nanoprisms formed in the initial 20-min iodide-free growth; (B) A SEM image of Au dodecagonal structures formed after a further 30-min growth from (A) in the presence of KI; (C) A SEM image of Au nanostars formed after another 30-min growth from (B) in the

presence of KI. Scale bars in all SEM images correspond to 100 nm. (D) A schematic showing the preferential etching (red arrows) at high-index edges that caused nonuniform growths (blue arrows) along different lateral directions to form Au nanostars. Nanostructures shown in (A), (B), and (C) were isolated from the same batch of synthesis at corresponding time points.

Furthermore, high-angle annular dark-field (HAADF) atomic-resolved scanning transmission electron microscopy (STEM) images identified that those Au dodecagonal nanostructures exhibited alternatively arranged low-index edges and high-index edges (Figures 4, S7, and S8, Table S1), in which low-index edges were preserved from initial Au nanoprisms (Figure 4A) and high-index edges corresponded to new intersecting edges formed from the truncated corners (Figures 4B and 4C). Those high-index facets with more low-coordinated sites were expected to serve as active sites for hot-hole-driven oxidative etching of Au^0 and reduce the deposition rate of Au^0. Thus, nonuniform deposition rates along different growth directions would lead low-index edges to evolve into tips (faster growth, Figure S9A) and high-index edges to trenches (slower growth) to form Au nanostars. Indeed, after another 30-min growth, we observed that those dodecagonal structures grew into Au nanostars (Figures 3C, 3D, S6C, S6D and S9B).

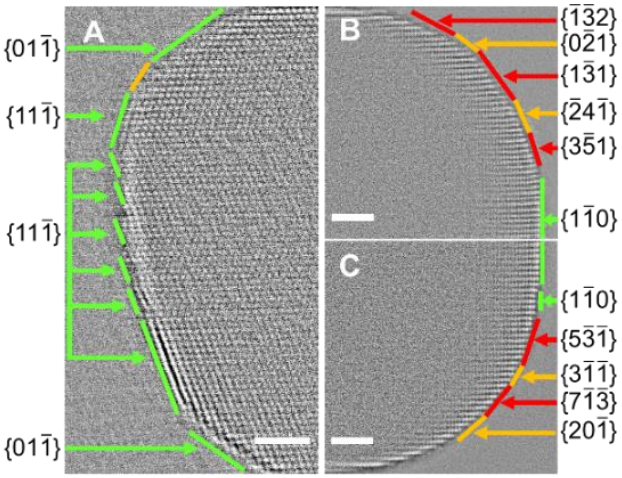

Figure 4. Filtered HAADF-STEM images along two edges of a single dodecagonal intermediate nanostructure (see Figure S7 for more details). (A) A filtered HAADF-STEM image of one edge acquired along [011] zone axis. This edge is dominated by low-index facets as indicated in the figure. (B) and (C) Filtered HAADF-STEM images of another edge acquired along [112] zone axis. This edge is dominated by high-index facets. Green lines in (A), (B), and (C) denote the location of low-index facets, while red and orange lines denote the location of high-index facets. Red and orange lines were used in alternative for a clearer view. It should be noted that in (A), facets with same indices align along different directions because of the existence of twin boundaries (i.e., a mirror plane). Scale bars in (A), (B), and (C) all represent 2 nm.

In summary, we have demonstrated that the synergy between plasmon-generated hot carriers and surface adsorbates provided a unique control over the anisotropic growth of plasmonic nanostructures. More importantly, we discovered that iodide assisted the hot-hole-driven oxidative etching of Au seed nanoparticles preferentially at edges with high-index facets to counteract the hot-electron-driven Au^0 deposition, leading to nonuniform growths along different lateral directions to form Au nanostars. Elucidating the essential function of plasmon-generated hot holes in our studies affirmed that both hot holes and hot electrons can be utilized in the light-driven synthesis of nanostructures. Moreover, it should be noted that the discovered cooperation of hot holes and iodide in our plasmonic system can be extended to general photo-excited processes. For instance, Au nanostars were also obtained by directly exciting the interband transition of planar-twinned seeds using blue light (470 ± 10 nm) in the presence of bromide (Figures S10 and S11). Taken together, our studies provide a comprehensive description of the interaction between hot carriers and surface adsorbates, and illustrate its great potential in regulating photochemical processes.

AUTHOR INFORMATION

Corresponding Author

*Email: wei@chem.ufl.edu

Present Addresses

[§]Yuchao Zhang: Key Laboratory of Photochemistry, CAS Research/Education Center for Excellence in Molecular Sciences, Institute of Chemistry, Chinese Academy of Sciences, Beijing 100190, P. R. China

Notes

The authors declare no competing financial interests.

ACKNOWLEDGMENT

This work is supported by the National Science Foundation under Grant CHE-1808539 and DMR-1352328. SEM characterization was conducted at MAIC and NRF, College of Engineering Research Service Centers, University of Florida. STEM characterization was performed at Material Measurement Laboratory of National Institute of Standards and Technology. W.G. especially appreciates the support of a graduate school fellowship from the University of Florida and the Department of Energy (DOE) Science Graduate Student Research (SCGSR) award.

REFERENCES

(1) Jin, R.; Charles Cao, Y.; Hao, E.; Métraux, G. S.; Schatz, G. C.; Mirkin, C. A. Controlling anisotropic nanoparticle growth through plasmon excitation. *Nature* **2003,** *425*, 487-490.

(2) Xue, C.; Métraux, G. S.; Millstone, J. E.; Mirkin, C. A. Mechanistic Study of photomediated triangular silver nanoprism Growth. *J. Am. Chem. Soc.* **2008,** *130*, 8337-8344.

(3) Jin, R.; Cao, Y.; Mirkin, C. A.; Kelly, K. L.; Schatz, G. C.; Zheng, J. G. Photoinduced conversion of silver nanospheres to nanoprisms. *Science* **2001,** *294*, 1901-1903.

(4) Langille, M. R.; Personick, M. L.; Mirkin, C. A. Plasmon-mediated syntheses of metallic nanostructures. *Angew. Chem., Int. Ed.* **2013,** *52*, 13910-13940.

(5) Langille, M. R.; Zhang, J.; Mirkin, C. A. Plasmon-mediated synthesis of heterometallic nanorods and icosahedra. *Angew. Chem., Int. Ed.* **2011,** *50*, 3543-3547.

(6) Golze, S. D.; Hughes, R. A.; Rouvimov, S.; Neal, R. D.; Demille, T. B.; Neretina, S. Plasmon-mediated synthesis of periodic arrays of gold nanoplates using substrate-immobilized seeds lined with planar defects. *Nano Lett.* **2019,** *19*, 5653-5660.

(7) Zhai, Y.; DuChene, J. S.; Wang, Y. C.; Qiu, J.; Johnston-Peck, A. C.; You, B.; Guo, W.; DiCiaccio, B.; Qian, K.; Zhao, E. W.; Ooi, F.; Hu, D.; Su, D.; Stach, E. A.; Zhu, Z.; Wei, W. D. Polyvinylpyrrolidone-induced anisotropic growth of gold nanoprisms in plasmon-driven synthesis. *Nat. Mater.* **2016,** *15*, 889-895.

(8) Khorashad, L. K.; Besteiro, L. V.; Correa-Duarte, M. A.; Burger, S.; Wang, Z. M.; Govorov, A. O. Hot electrons generated in chiral plasmonic nanocrystals as a mechanism for surface photochemistry and chiral growth. *J. Am. Chem. Soc.* **2020,** *142*, 4193-4205.

(9) Zhai, Y.; Zhang, F.; Zhang, B.; Gao, X. Engineering single nanopores on gold nanoplates by tuning crystal screw dislocation. *Adv. Mater.* **2017,** *29*, 1703102.

(10) Redmond, P. L.; Brus, L. E. "Hot electron" photo-charging and electrochemical discharge dinetics of silver nanocrystals. *J. Phys. Chem. C* **2007,** *111*, 14849-14854.

(11) Redmond, P. L.; Wu, X.; Brus, L. Photovoltage and photocatalyzed growth in citrate-stabilized colloidal silver nanocrystals. *J. Phys. Chem. C* **2007,** *111*, 8942-8947.

(12) Wu, X.; Redmond, P. L.; Liu, H.; Chen, Y.; Steigerwald, M.; Brus, L. Photovoltage mechanism for room light conversion of citrate stabilized silver canocrystal seeds to large nanoprisms. *J. Am. Chem. Soc.* **2008,** *130*, 9500-9506.

(13) Wu, X.; Thrall, E. S.; Liu, H.; Steigerwald, M.; Brus, L. Plasmon induced photovoltage and charge separation in citrate-stabilized gold nanoparticles. *J. Phys. Chem. C* **2010,** *114*, 12896-12899.

(14) Thrall, E. S.; Preska Steinberg, A.; Wu, X.; Brus, L. E. The role of photon energy and semiconductor substrate in the plasmon-mediated photooxidation of citrate by silver nanoparticles. *J. Phys. Chem. C* **2013,** *117*, 26238-26247.

(15) Maillard, M.; Huang, P.; Brus, L. Silver nanodisk growth by surface plasmon enhanced photoreduction of adsorbed [Ag^+]. *Nano Lett.* **2003,** *3*, 1611-1615.

(16) DuChene, J. S.; Niu, W.; Abendroth, J. M.; Sun, Q.; Zhao, W.; Huo, F.; Wei, W. D. Halide anions as shape-directing agents for obtaining high-quality anisotropic gold nanostructures. *Chem. Mater.* **2012,** *25*, 1392-1399.

(17) Wang, J.; Li, Y. F.; Huang, C. Z. Identification of iodine-induced morphological transformation of gold nanorods. *J. Phys. Chem. C* **2008,** *112*, 11691-11695.

(18) Millstone, J. E.; Wei, W.; Jones, M. R.; Yoo, H.; Mirkin, C. A. Iodide ions control seed-mediated growth of anisotropic gold nanoparticles. *Nano Lett.* **2008,** *8*, 2526-2529.

(19) Liu, S.; Niu, W.; Firdoz, S.; Zhang, W. Iodide-switched deposition for the synthesis of segmented Pd-Au-Pd nanorods: crystal facet matters. *Langmuir* **2017,** *33*, 12254-12259.

(20) Meena, S. K.; Celiksoy, S.; Schafer, P.; Henkel, A.; Sönnichsen, C.; Sulpizi, M. The role of halide ions in the anisotropic growth of gold nanoparticles: a microscopic, atomistic perspective. *Phys. Chem. Chem. Phys.* **2016,** *18*, 13246-13254.

(21) Ha, T. H.; Koo, H.-J.; Chung, B. H. Shape-controlled syntheses of gold nanoprisms and nanorods influenced by specific adsorption of halide ions. *J. Phys. Chem. C* **2007,** *111*, 1123-1130.

(22) Brongersma, M. L.; Halas, N. J.; Nordlander, P. Plasmon-induced hot carrier science and technology. *Nat. Nanotechnol.* **2015,** *10*, 25-34.

(23) Wang, D.; Koh, Y. R.; Kudyshev, Z. A.; Maize, K.; Kildishev, A. V.; Boltasseva, A.; Shalaev, V. M.; Shakouri, A. Spatial and temporal nanoscale plasmonic heating quantified by thermoreflectance. *Nano Lett.* **2019,** *19*, 3796-3803.

(24) Zou, N.; Chen, G.; Mao, X.; Shen, H.; Choudhary, E.; Zhou, X.; Chen, P. Imaging catalytic hotspots on single plasmonic nanostructures via correlated super-resolution and electron microscopy. *ACS Nano* **2018,** *12*, 5570-5579.

(25) Fujiwara, H.; Suzuki, T.; Pin, C.; Sasaki, K. Localized ZnO growth on a gold nanoantenna by plasmon-assisted hydrothermal synthesis. *Nano Lett.* **2020,** *20*, 389-394.

(26) Baffou, G.; Quidant, R. Thermo-plasmonics: using metallic nanostructures as nano-sources of heat. *Laser Photonics Rev.* **2013,** *7*, 171-187.

(27) Matsuura, T.; Imaeda, K.; Hasegawa, S.; Suzuki, H.; Imura, K. Characterization of overlapped plasmon modes in a gold hexagonal plate revealed by three-dimensional near-field optical microscopy. *J. Phys. Chem. Lett.* **2019,** *10*, 819-824.

(28) Kim, Y.; Smith, J. G.; Jain, P. K. Harvesting multiple electron-hole pairs generated through plasmonic excitation of Au nanoparticles. *Nat. Chem.* **2018,** *10* (7), 763-769.

(29) Schlather, A. E.; Manjavacas, A.; Lauchner, A.; Marangoni, V. S.; DeSantis, C. J.; Nordlander, P.; Halas, N. J. Hot hole photoelectrochemistry on Au@SiO_2@Au nanoparticles. *J. Phys. Chem. Lett.* **2017,** *8*, 2060-2067.

(30) Brown, A. M.; Sundararaman, R.; Narang, P.; Goddard, W. A., III; Atwater, H. A. Nonradiative plasmon decay and hot carrier dynamics: effects of phonons, surfaces, and geometry. *ACS Nano* **2016,** *10*, 957-966.

(31) Barman, T.; Hussain, A. A.; Sharma, B.; Pal, A. R. Plasmonic hot hole generation by interband transition in gold-polyaniline. *Sci. Rep.* **2015,** *5*, 18276.

(32) Sundararaman, R.; Narang, P.; Jermyn, A. S.; Goddard, W. A., III; Atwater, H. A. Theoretical predictions for hot-carrier generation from surface plasmon decay. *Nat. Commun.* **2014,** *5*, 5788.

(33) Bernardi, M.; Mustafa, J.; Neaton, J. B.; Louie, S. G. Theory and computation of hot carriers generated by surface plasmon polaritons in noble metals. *Nat. Commun.* **2015,** *6*, 7044.

(34) Zhang, Y.; He, S.; Guo, W.; Hu, Y.; Huang, J.; Mulcahy, J. R.; Wei, W. D. Surface-plasmon-driven hot electron photochemistry. *Chem. Rev.* **2018,** *118*, 2927-2954.

(35) Marrani, A. G.; Bonomo, M.; Dini, D. Adsorption dynamics of redox active species onto polarized surfaces of sensitized NiO. *ACS Omega* **2019,** *4*, 1690-1699.

(36) Bella, F.; Popovic, J.; Lamberti, A.; Tresso, E.; Gerbaldi, C.; Maier, J. Interfacial effects in solid-liquid electrolytes for improved stability and performance of dye-sensitized solar cells. *ACS Appl. Mater. Interfaces* **2017,** *9*, 37797-37803.

(37) Shin, H.; Kim, B.-M.; Jang, T.; Kim, K. M.; Roh, D.-H.; Nam, J. S.; Kim, J. S.; Kim, U.-Y.; Lee, B.; Pang, Y.; Kwon, T.-H. Surface state-mediated charge transfer of Cs_2SnI_6 and its application in dye-sensitized solar cells. *Adv. Energy Mater.* **2019,** *9*, 1803243.

(38) Zhao, J.; Nguyen, S. C.; Ye, R.; Ye, B.; Weller, H.; Somorjai, G. A.; Alivisatos, A. P.; Toste, F. D. A Comparison of Photocatalytic activities of gold nanoparticles following plasmonic and interband excitation and a strategy for harnessing interband hot carriers for solution phase photocatalysis. *ACS Cent. Sci.* **2017,** *3*, 482-488.

(39) Al-Zubeidi, A.; Hoener, B. S.; Collins, S. S. E.; Wang, W.; Kirchner, S. R.; Hosseini Jebeli, S. A.; Joplin, A.; Chang, W. S.; Link, S.; Landes, C. F. Hot Holes Assist Plasmonic Nanoelectrode Dissolution. *Nano. Lett.* **2019,** *19*, 1301-1306.

(40) Thambi, V.; Kar, A.; Ghosh, P.; Khatua, S. Light-controlled in situ bidirectional tuning and monitoring of gold nanorod plasmon via oxidative etching with $FeCl_3$. *J. Phys. Chem. C* **2018,** *122*, 24885-24890.

(41) Saito, K.; Tanabe, I.; Tatsuma, T. Site-selective plasmonic etching of silver nanocubes. *J. Phys. Chem. Lett.* **2016,** *7*, 4363-4368.

(42) Hoener, B. S.; Byers, C. P.; Heiderscheit, T. S.; De Silva Indrasekara, A. S.; Hoggard, A.; Chang, W.-S.; Link, S.; Landes, C. F. Spectroelectrochemistry of halide anion adsorption and dissolution of single gold nanorods. *J. Phys. Chem. C* **2016,** *120*, 20604-20612.

(43) Magnussen, O. M. Ordered anion adlayers on metal electrode surfaces. *Chem. Rev.* **2002,** *102*, 679-726.

(44) Almora-Barrios, N.; Novell-Leruth, G.; Whiting, P.; Liz-Marzán, L. M.; López, N. Theoretical description of the role of halides, silver, and surfactants on the structure of gold nanorods. *Nano Lett.* **2014,** *14*, 871-875.

(45) Li, W. L.; Li, Y.; Xu, C. Q.; Wang, X. B.; Vorpagel, E.; Li, J. Periodicity, electronic structures, and bonding of gold tetrahalides $[AuX_4]^-$ (X = F, Cl, Br, I, At, Uus). *Inorg. Chem.* **2015,** *54*, 11157-11167.

(46) Scanlon, M. D.; Peljo, P.; Méndez, M. A.; Smirnov, E.; Girault, H. H. Charging and discharging at the nanoscale: Fermi level equilibration of metallic nanoparticles. *Chem. Sci.* **2015,** *6*, 2705-2720.

(47) Grätzel, M. Photoelectrochemical cells. *Nature* **2001,** *414*, 338-344.

(48) Aylmore, M. G. Chapter 27 - Alternative lixiviants to cyanide for leaching gold ores. In *Gold Ore Processing*, second edition, Adams, M. D., Ed.; Elsevier: Cambridge, MA, 2016; pp 447-484.

(49) Villarreal, E.; Li, G. G.; Zhang, Q.; Fu, X.; Wang, H. Nanoscale surface curvature effects on ligand-nanoparticle interactions: a plasmon-enhanced spectroscopic study of thiolated ligand adsorption, desorption, and exchange on gold nanoparticles. *Nano Lett.* **2017,** *17*, 4443-4452.

(50) Kim, S. Y.; Dae, K. S.; Koo, K.; Kim, D.; Park, J.; Yuk, J. M. Sequential growth and etching of gold nanocrystals revealed by high-resolution liquid electron microscopy. *Phys. Status Solidi A*, **2019,** *216*, 1800949

(51) Yuan, H.; Janssen, K. P. F.; Franklin, T.; Lu, G.; Su, G.; Su, L.; Gu, X.; Uji-I, H.; Roeffaers, M. B. J.; Hofken, J. Reshaping anisotropic gold nanoparticles through oxidative etching: the role of the surfactant and nanoparticle surface curvature. *RSC Adv.* **2015,** *5*, 6829-6833.

Cooperation of Hot Holes and Surface Adsorbates in Plasmon-Driven Anisotropic Growth of Gold Nanostars

Wenxiao Guo,[†] Aaron C. Johnston-Peck,[‡] Yuchao Zhang,[†,§] Yue Hu,[†] Jiawei Huang,[†] and Wei David Wei[†]*

[†]Department of Chemistry and Center for Catalysis, University of Florida, Gainesville, Florida 32611, United States

[‡]Material Measurement Laboratory, National Institute of Standards and Technology, 100 Bureau Drive, Gaithersburg, Maryland 20899, United States

[§]Present address: Key Laboratory of Photochemistry, CAS Research/Education Center for Excellence in Molecular Sciences, Institute of Chemistry, Chinese Academy of Sciences, Beijing 100190, P. R. China

*Address correspondence to wei@chem.ufl.edu

Experimental Procedures

Materials

Gold (III) chloride trihydrate ($HAuCl_4$), polyvinylpyrrolidone (PVP, Mw = 40,000 Da), and potassium iodide (KI) were purchased from Sigma Aldrich. Methanol (99.8 %) was obtained from Fisher Chemicals. All synthesis processes were performed with Nanopure water (18.2 MΩ). All glassware was cleaned with *aqua regia* solution and rinsed thoroughly with Nanopure water before use (caution! *Aqua regia* is highly corrosive and toxic: handle with care and use appropriate personal protection equipment).

Instrumentation

The light source used for the plasmon-driven growth of Au nanostars was a halogen lamp (Dolan-Jenner MI-150) equipped with an internal IR holder/filter (to avoid excessive heating). Single-wavelength bandpass filters were purchased from Thorlabs. Ultraviolet-visible-near infrared (UV-Vis-NIR) spectra of products were collected using a Shimadzu UV-2600 spectrophotometer. Scanning electron microscopy (SEM) images of Au nanostars were collected using a FEI Nova Nano 430 SEM at the Nanoscale Research Facility of the University of Florida. Selected area electron diffraction (SAED) patterns and high-angle annular dark-field (HAADF) scanning transmission electron microscopy

(STEM) images were acquired from a transmission electron microscope (TEM) operated at an accelerating voltage of 300 kV at Material Measurement Laboratory of National Institute of Standards and Technology *(Note: Certain commercial equipment, instruments, or materials are identified in this paper in order to specify the experimental procedure adequately. Such identification is not intended to imply recommendation or endorsement by the National Institute of Standards and Technology, nor is it intended to imply that the materials or equipment identified are necessarily the best available for the purpose.).* The probe forming optics of the instrument was aberration-corrected, and the convergence angle was set to approximately 13.5 mrad. HAADF-STEM images were acquired using a Fischione Model 3000 detector, in which the inner collection angle was set to approximately either 58 mrad or 71 mrad. Electrochemical experiments were conducted using an Autolab potentiostat (PGSTAT302N) from Metrohm. Light sources used in electrochemical experiments were single-wavelength LEDs (470 nm and 530 nm) with a maximum power density of 240 mW/cm^2.

Experimental details

Synthesis of Au nanostars:

Au seeds were synthesized using a previously reported method.[1,2] The seed solution was aged for more than two weeks before use. To synthesize Au nanostars, a solution containing 5 mL of H_2O, 500 μL of 5 mg/mL PVP solution, 500 μL of methanol, 400 μL of 10 mM $HAuCl_4$ solution, and 1 μL of aged seed solution was prepared (i.e., growth solution). The seed solution contained a mixture of planar-twinned seeds and penta-twinned seeds, while only planar-twinned seeds can lead to the formation of Au nanostars.[1] To isolate planar-twinned Au seeds from the mixture, the growth solution was incubated in a water bath at 24.5 °C under the dark condition for 24 h. Penta-twinned Au seeds were reported to grow faster in the dark and would gain a heavier mass after the incubation.[1] The incubated growth solution was then centrifuged at 10,000 rpm for 10 min, allowing for the precipitation of penta-twinned seeds. The supernatant of the growth solution after the centrifugation contained mainly planar-twinned seeds and was then transferred to a glass

vial with a Teflon-lined cap for the plasmon-driven growth. The growth solution was irradiated by a halogen lamp equipped with a 520 ±10 nm bandpass filter at 3.4 mW/cm^2. After 20 min of irradiation, 20 μL of 1 mM KI solution was injected into the growth solution (overall KI concentration: 4 μM). The solution was then irradiated for another 60 min to complete the growth. The growth in the dark was carried out by storing the incubated and centrifuged growth solution in the dark at 50 ℃ for 24 h.

Wavelength-dependent growth

Wavelength-dependent growth was carried out after the incubation and centrifugation of a growth solution. It should be noted that small planar-twinned Au seeds in the growth solution only had strong absorption near 520 nm,[1] so that the growth would not happen if the growth solution was irradiated with wavelengths too far from 520 nm from the beginning of plasmon-driven synthesis. Instead, the growth solution was first irradiated at 520 ± 10 nm for 20 min in the absence of iodide. This initial growth step enabled planar-twinned Au seeds to develop into anisotropic (prism-like) structures that exhibited a broader SPR absorption band.[1] After this initial growth, KI was added to the growth solution, and the mixture was irradiated using bandpass filters with targeting wavelength (from 460 nm to 640 nm) continuously for another 60 min.

Electrochemical measurements:

Electrochemical measurements were carried out in a three-electrode electrochemical cell with a Pt wire counter electrode and a Ag/AgCl (3.5 M KCl) reference electrode. The working electrode was a Au nanocrystal electrode, which was fabricated by sputtering 10 nm of Au film on a FTO electrode and then calcinating for 2 h at 600 ℃. All electrochemical experiments were conducted in 50 mL of 0.5 M $NaClO_4$ with a pH value tuned to 3.0 using $HClO_4$ (i.e., the pH of the growth solution). To modify the Au nanocrystal electrode with iodide, the working electrode was immersed in a 0.5 M $NaClO_4$ solution containing KI until its rest potential became stable. The PVP-adsorbed electrode was prepared by immerging a Au nanocrystal electrode in a 20 mg/mL PVP solution overnight and then rinsing with water.

Edge facets identification using STEM:

Dodecagonal intermediates obtained during the growth of Au nanostars were isolated from the growth solution and loaded on a C-supported Cu grid. Amorphous silica particles were deposited prior to the deposition of Au nanostars to tilt Au nanostars for imaging their edges. As shown in Figure S1, the microscope stage was tilted in the STEM chamber to orient the nanostructure to an "edge-on" pattern, in which the edge of interest was aligned with the incident electron beam. The obtained STEM images were filtered using a "Trend Substrate" filter (HREM-Filters Lite version 3.0, HREM Research Inc.) as implemented in Digital Micrograph (Gatan Inc.) to enhance the visualization of atomic columns. The filter removed the low-frequency component of the image (background) that was prominent due to the combination of a high atomic number and a large sample thickness. Facets exposed on edges were then identified by matching the arrangement of atoms with that of characteristic crystal models.

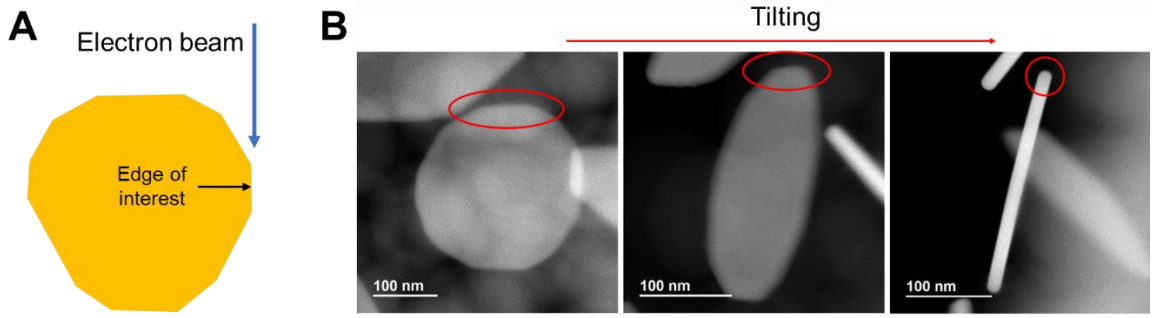

Figure S1. The process of obtaining the atomic-resolved STEM image of an edge of a dodecagonal structure. (A) A schematic showing the orienting of Au nanostructures for measuring edge facets. The sample stage was tilted until the edge of interest aligned with the incident electron beam (blue arrow). (B) An example of the tilting process to align a nanostructure. The red circle indicated the edge to be imaged.

Supplementary Figures and Tables

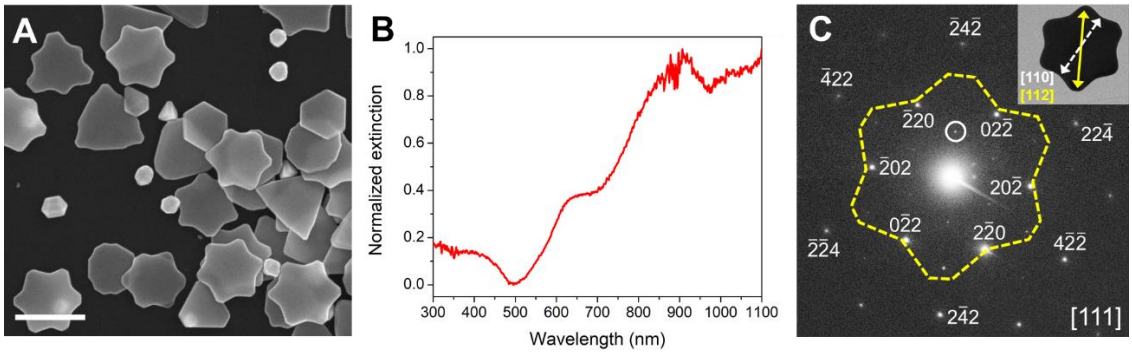

Figure S2. Characterizations of Au nanostars. (A) A low-magnification SEM image of Au nanostars. The scale bar represented 500 nm. (B) The UV-Vis spectrum obtained from an aqueous suspension of Au nanostars. The peak at ca. 900 nm stemmed from the Au nanostars, and the shoulder peak at ca. 600 nm originated from the small population of Au NPs grown from the penta-twinned Au seeds that remained in the growth solution after incubation and centrifugation. (C) A SAED pattern collected from a Au nanostar (corresponding TEM image shown in the inset) lying flat on a Cu grid. The pattern was indexed to a [111] zone axis, suggesting that the top and bottom surfaces of the nanostar are terminated by {111} facets, which was confirmed by atomic resolution HAADF-STEM imaging (not shown). {422} and {220} Bragg reflections were labelled. A forbidden $\frac{1}{3}${422} Bragg reflection marked by the white circle indicated the presence of planar defects.[3-6] Crystallographic directions within Au nanostars were extracted from the SAED pattern. As indicated in the inset TEM image, tips of Au nanostars grew along [112] directions (yellow solid arrows), and trenches grew along [110] directions (white dashed arrows). Only one pair of tips and trenches were labeled for a clearer view.

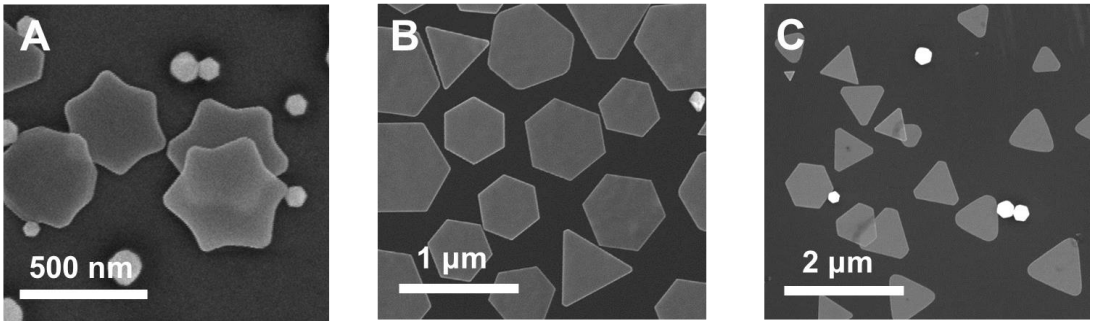

Figure S3. SEM images of Au nanostructures formed under different experimental conditions. (A) Au nanostars formed from the plasmon-driven growth in the presence of 4 μM of NaI. (B) Regular nanoprisms formed from the plasmon-driven growth in the absence of iodide. (C) Regular nanoprisms formed from the growth in the dark in the presence of iodide.

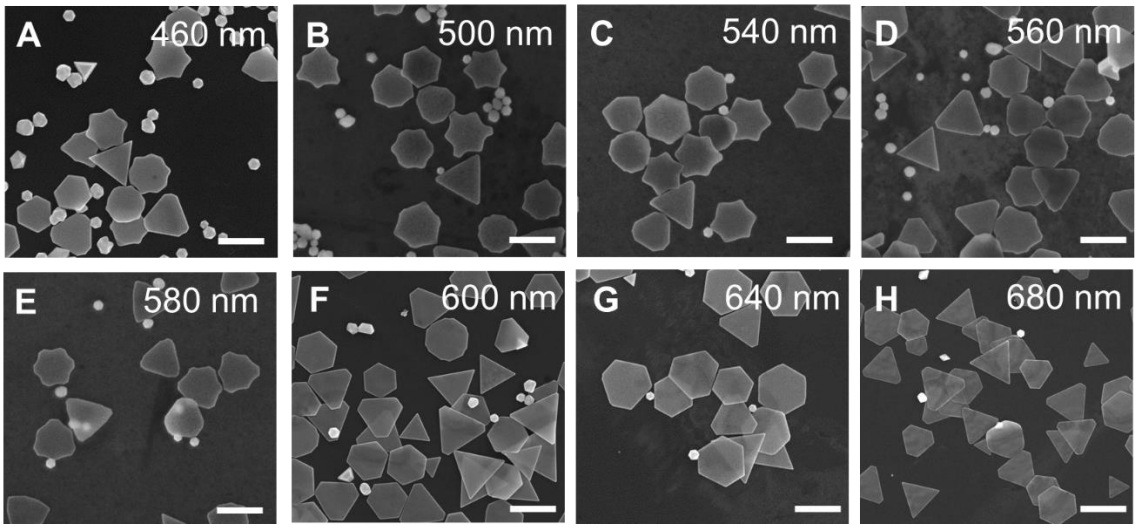

Figure S4. SEM images of Au nanostructures formed from the plasmon-driven growth with different irradiation wavelengths. (A) – (E) Au nanostars formed when shorter wavelengths (< 600 nm, 3.4 mW/cm^2) were used. (F) – (H) Regular Au nanoprisms formed when longer wavelengths (≥ 600 nm, 3.4 mW/cm^2) were used. Scale bars stand for 500 nm in all figures.

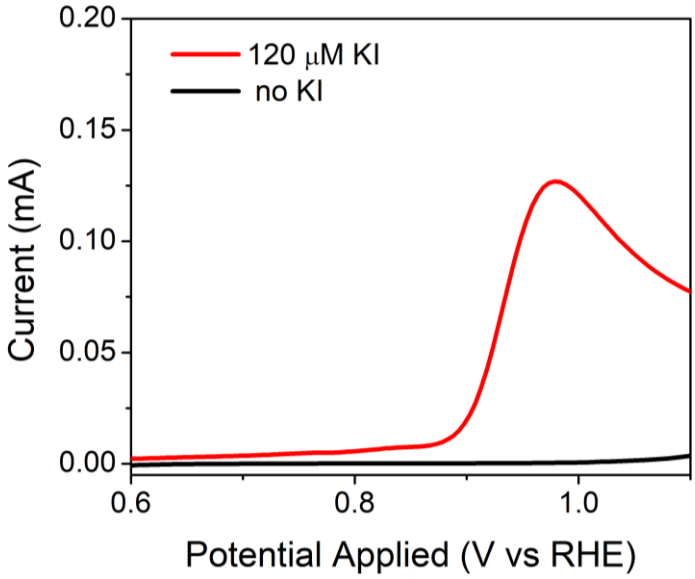

Figure S5. A linear sweep voltammetry (LSV) scan obtained on Au nanocrystal electrodes in the presence (red curve) and absence (black curve) of 120 μM KI. A peak at ca. 0.95 V vs. RHE was observed for the iodide-adsorbed electrode, which originated from the one-electron oxidation of Au^0 to AuI_2^-.[7]

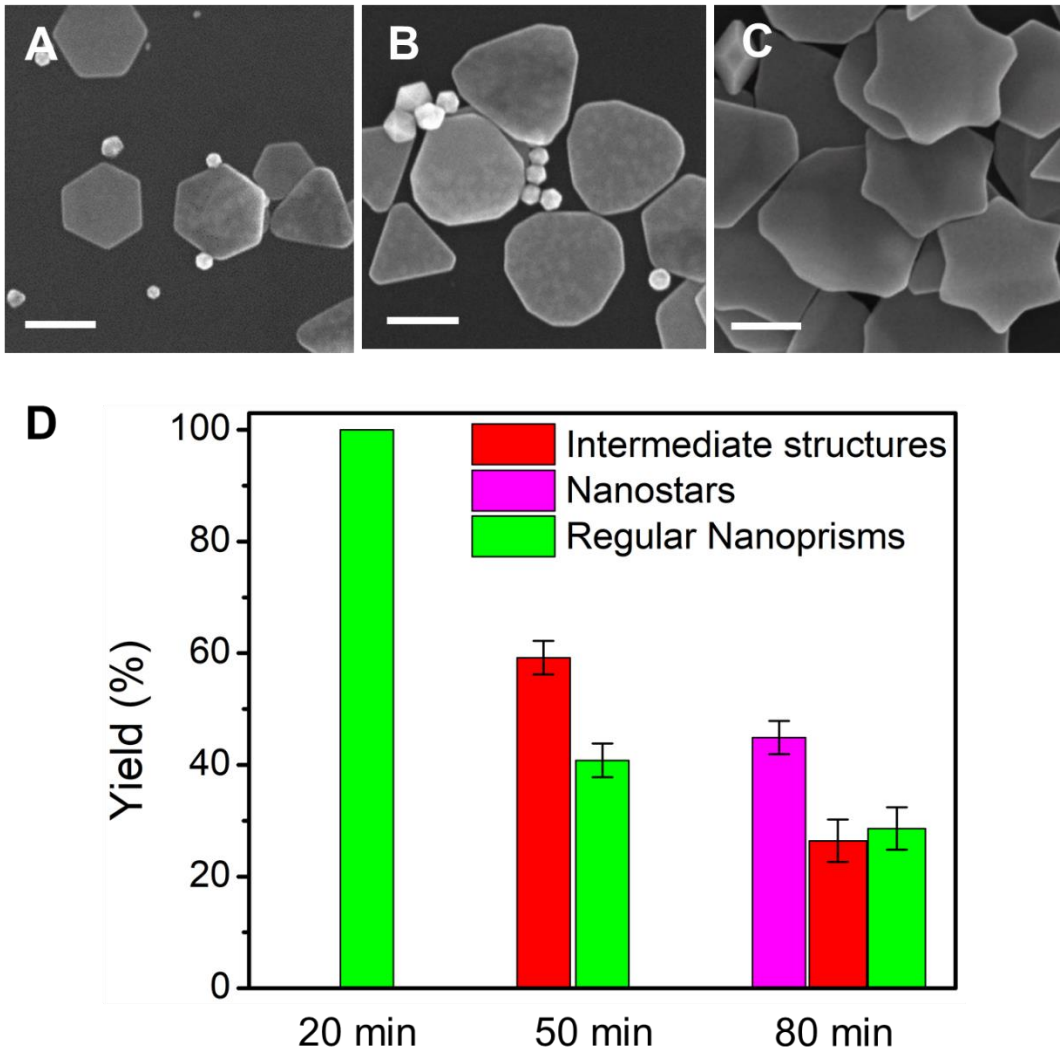

Figure S6. SEM images showing the ensemble of Au nanostructures during the plasmon-driven growth in the presence of iodide after (A) 20 minutes, (B) 50 minutes, and (C) 80 minutes of growth. (D) A statistical analysis of products formed at each stage. The yield of dodecagonal intermediate structures at 50 min was 59 ± 3%, and the yield of nanostars at 80 min was 45 ± 3%. Over 200 nanostructures were counted at each stage to obtain the distribution of structures. Scale bars in all (A), (B), and (C) stand for 200 nm.

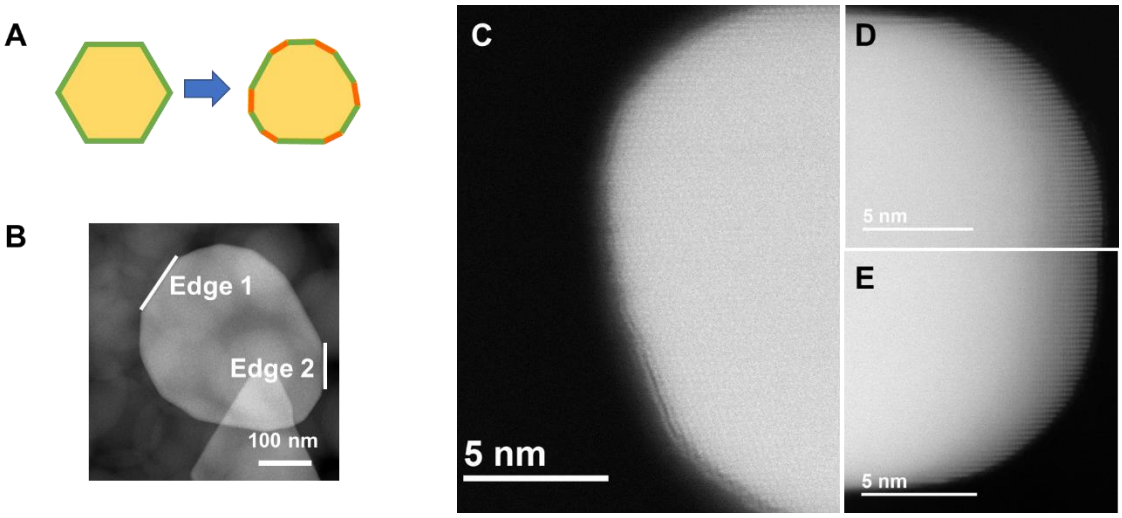

Figure S7. Facet identification of the intermediate structure formed during the growth of Au nanostars. (A) A schematic showing the truncation of a regular Au nanoprism to form the dodecagonal intermediate. Edges marked with green color were composed of low-index facets that are typical for Au nanoprisms, and edges marked with orange color were newly formed intersecting edges with high-index facets. Two types of edges were arranged alternatively. (B) Indication of the position of two edges on an individual dodecagonal intermediate structure examined by STEM. By arrangement, edge 1 and edge 2 represented those two types of edges shown in (A). (C) HAADF-STEM images along edge 1 of the intermediate dodecahedral structure. (D) and (E) HAADF-STEM images along edge 2 of the intermediate dodecahedral structure. (C), (D), and (E) are unfiltered copies corresponding to images shown in Figure 4A, 4B, and 4C of the main text, respectively. From the facet identification shown in Figure 4, it can be concluded that edge 1 corresponded to a low-index green edge in (A), and edge 2 corresponded to a high-index orange edge in (A).

The facet analysis was conducted on 13 edges from 10 dodecagonal structures. Two types of edges with drastically different percentages of low-index regions (i.e., Au {111}, {110}, and {100}) and high-index regions were identified (**Table S1**). The first type of edges had approximately 68% low-index components, while the second type of edges only had about

23% low-index component. Edges with more high-index components corresponded to active sites for hot-hole-induced etching of Au^0.

Table S1. Summary of edge facets of dodecagonal intermediates

Structure #	Low-index component (%)	High-index ratio component (%)
Type 1		
1	62.5	37.5
2	68.9	31.1
3	66.1	33.9
4	72.8	27.2
5	74.3	25.7
6	71.3	28.7
7	69.4	30.6
8	65.5	34.5
9	63.8	36.2
10	66.6	33.4
Average	68.1 ± 3.9	31.9 ± 3.9
Type 2		
11	20.8	79.2
12	20.0	80.0
13	28.7	71.3

Average	23.2 ± 4.8	76.8 ± 4.8

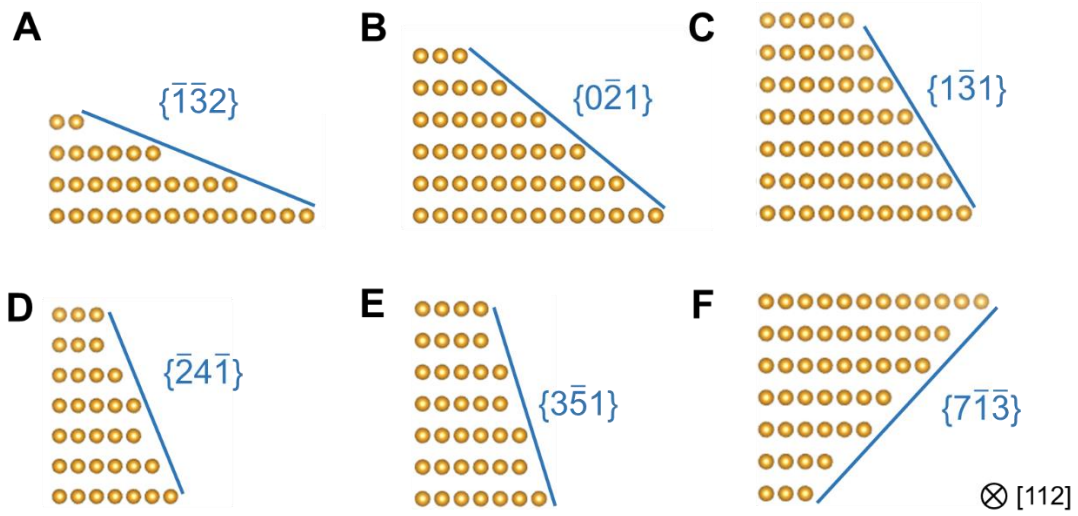

Figure S8. Schematics of high-indexed facets observed on dodecagonal intermediates as viewed along the [112] direction.

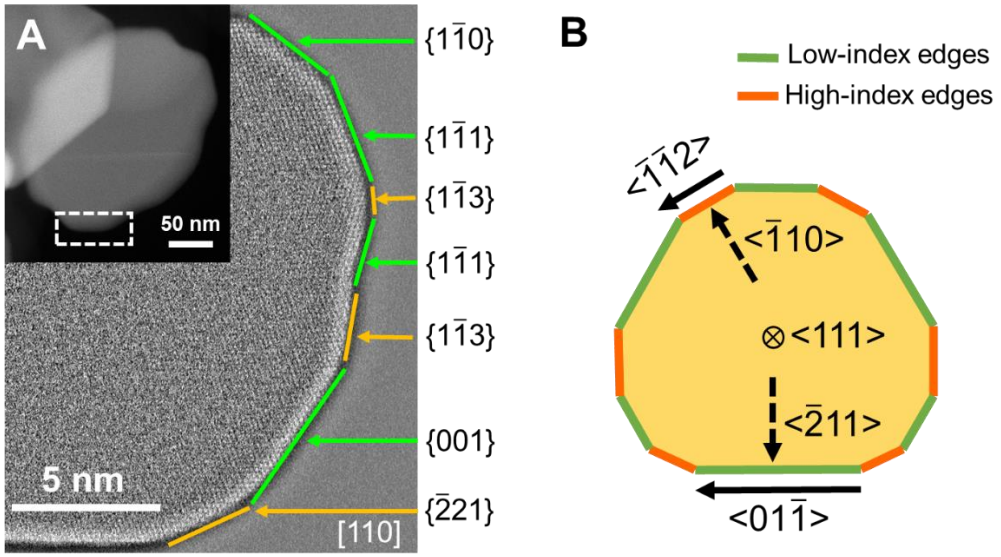

Figure S9. Growth of dodecagonal intermediate nanostructures into Au nanostars. (A) A HAADF-STEM image of an early-stage nanostar's tip (indicated by the dashed frame). The tip mainly consisted of low-index facets, which indicated the faster growth of edges dominated by low-index facets of intermediate structures, confirming that tips of Au nanostars evolved from low-index edges of dodecagonal intermediate nanostructures. (B) Derived crystallographic directions within a dodecagonal intermediate nanostructure. As indicated in Figure 4 in the main text, zone axes used to obtain HAADF-STEM images on a low-index edge and a high-index edge were [110] and [112] (i.e., paralleled to chosen edges), respectively. Since the top and bottom faces of those dodecagonal intermediate nanostructures were bound by {111} facet, it can be derived from the crystal structure of Au that low-index edges grew along [112] directions and high-index edges grew along [110] directions, which matched with growth direction of tips (i.e., [112]) and trenches (i.e., [110]) of nanostars (Figure S2B), respectively. This match in growth directions indicated that tips of nanostars evolved from low-index facets and trenches evolved from high-index facets.

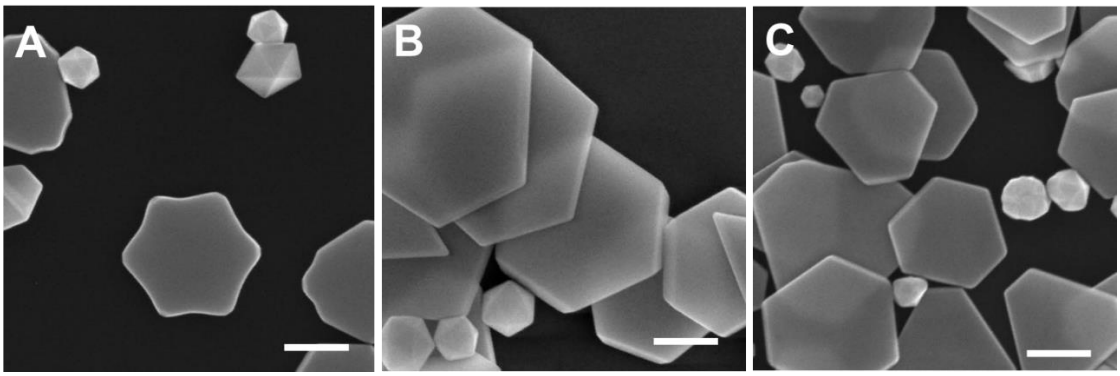

Figure S10. SEM images showing the plasmon-driven synthesis of Au nanostars in the presence of KBr. (A) The formation of Au nanostars in the presence of 0.2 mM KBr under 460 nm irradiation. (B) The formation of regular Au nanoprisms in the presence of 4 μM KBr under 460 nm irradiation. (C) The formation of regular Au nanoprisms in the presence of 0.2 mM KBr under 560 nm irradiation. It can be seen that to obtain Au nanostars using bromide, a higher concentration of KBr and the shorter-wavelength irradiation that directly

caused photoexcitation of Au (i.e., interband transitions) to form more d-band holes should be used. The scale bar stands for 200 nm in all images.

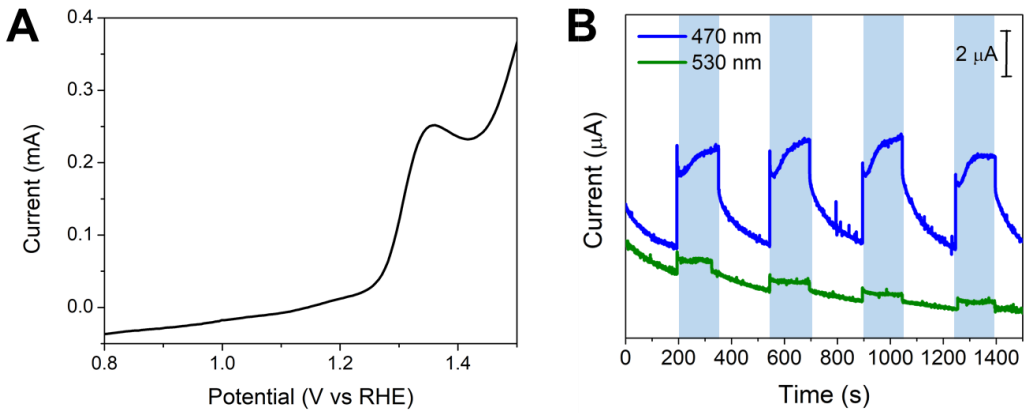

Figure S11. Photoelectrochemical results confirming the hot-hole-driven etching of Au^0 assisted by bromide. (A) A LSV scan obtained on a Au nanocrystal electrode in the presence of KBr. A peak at ca. 1.35 V vs. RHE stood for the one-electron oxidation of Au^0 to $AuBr_2^-$.[7] (B) I-t curves collected at 1.40 V vs. RHE showing the anodic photocurrent of a Au electrode in the presence of bromide. Shaded regions in (B) represented the light irradiation using either 530 nm (green curve) or 470 ± 10 nm (blue curve) LED light source (240 mW/cm^2). A significant enhancement can be observed only when using the 470 nm irradiation.

References

(S1) DuChene, J. S.; Niu, W.; Abendroth, J. M.; Sun, Q.; Zhao, W.; Huo, F.; Wei, W. D. Halide anions as shape-directing agents for obtaining high-quality anisotropic gold nanostructures. *Chem. Mater.* **2012,** *25* (8), 1392-1399.

(S2) Zhai, Y.; DuChene, J. S.; Wang, Y. C.; Qiu, J.; Johnston-Peck, A. C.; You, B.; Guo, W.; DiCiaccio, B.; Qian, K.; Zhao, E. W.; Ooi, F.; Hu, D.; Su, D.; Stach, E. A.; Zhu, Z.; Wei, W. D. Polyvinylpyrrolidone-induced anisotropic growth of gold nanoprisms in plasmon-driven synthesis. *Nat. Mater.* **2016,** *15* (8), 889-895.

(S3) Langille, M. R.; Personick, M. L.; Mirkin, C. A. Plasmon-Mediated Syntheses of Metallic Nanostructures. *Angew. Chem., Int. Ed.* **2013,** *52* (52), 13910-13940.

(S4) Kirkland, A. I.; Jefferson, D. A.; Duff, D. G.; Edwards, P. P.; Gameson, I.; Johnson, B. F. G.; Smith, D. J. Structural studies of trigonal lamellar particles of gold and silver. *Proc. R. Soc. A* **1993,** *440* (1910), 589-609.

(S5) Carim, A. H.; Lew, K.-K.; Redwing, J. M. Bicrystalline silicon nanowires. *Adv. Mater.* **2001,** *13* (19), 1489-1491.
(S6) Germain, V.; Li, J.; Ingert, D.; Wang, Z. L.; Pileni, M. P. Stacking faults in formation of silver nanodisks. *J. Phys. Chem. B* **2003,** *107* (34), 8717-8720.

(S7) Aylmore, M. G. Chapter 27 - Alternative lixiviants to cyanide for leaching gold ores. In *Gold Ore Processing*, second edition, Adams, M. D., Ed.; Elsevier: Cambridge, MA, 2016; pp 447-484.